X-ray Timing Observations of PSR J1930+1852 in the Crab-like SNR G54.1+0.3

Fangjun Lu[1,2], Q.Daniel Wang[2], E. V. Gotthelf[3], and Jinlu Qu[1]

ABSTRACT

We present new X-ray timing and spectral observations of PSR J1930+1852, the young energetic pulsar at the center of the non-thermal supernova remnant G54.1+0.3. Using data obtained with the *Rossi* X-ray Timing Explorer (*RXTE*) and *Chandra* X-ray observatories we have derived an updated timing ephemeris of the 136 ms pulsar spanning 6 years. During this interval, however, the period evolution shows significant variability from the best fit constant spin-down rate of $\dot{P} = 7.5112(6) \times 10^{-13}$ s s^{-1}, suggesting strong timing noise and/or glitch activity. The X-ray emission is highly pulsed ($71 \pm 5\%$ modulation) and is characterized by an asymmetric, broad profile ($\sim 70\%$ duty cycle) which is nearly twice the radio width. The spectrum of the pulsed emission is well fitted with an absorbed power law of photon index $\Gamma = 1.2 \pm 0.2$; this is marginally harder than that of the unpulsed component. The total $2 - 10$ keV flux of the pulsar is 1.7×10^{-12} erg cm^{-2} s^{-1}. These results confirm PSR J1930+1852 as a typical Crab-like pulsar.

Subject headings: ISM: individual (G54.1+0.3)—ISM: jets and outflows—radiation mechanisms: non-thermal—stars:neutron (PSR J1930+1852)— supernova remnants—X-rays: ISM

[1]Laboratory of Particle Astrophysics, Institute of High Energy Physics, CAS, Beijing 100039, P.R. China; lufj@mail.ihep.ac.cn; qujl@mail.ihep.ac.cn

[2]Astronomy Department, University of Massachusetts, Amherst, MA 01003; wqd@astro.umass.edu

[3]Columbia Astrophysics Laboratory, Columbia University, 550 West 120th Street, New York, NY 10027; eric@astro.columbia.edu

1. Introduction

Young rotation-powered pulsars typically radiate a large fraction of their spin-down energy at X-ray energies. Observations in this band are thus important to the study of the spin-down evolution of such pulsars and their emission mechanism(s). The study also helps to understand the mechanical energy output of the pulsars into their surroundings, manifested as pulsar wind nebulae (PWNe). To this end, one needs to monitor the spin-down at various evolutionary stages of young pulsars and to measure their energy spectra, both pulsed and unpulsed, with various viewing angles. However, only a dozen or so of young pulsars with PWNe have been identified and studied in detailed so far.

The recently discovered 136 ms pulsar PSR J1930+1852 at the center of the supernova remnant (SNR) G54.1+0.3 is the latest example of a Crab-like pulsar (Camilo et al. 2002). Known as the "Bulls-Eye" pulsar, PSR J1930+1852 is surrounded by a bright symmetric ring of emission (Lu et al. 2002) similar to the toroidal and jet-like structure associated with the Crab pulsar, but viewed nearly face-on. Based on the initial timing parameters, PSR J1930+1852 is the eighth most energetic pulsar known, with a rotational energy loss rate of $\dot{E} = 1.2 \times 10^{37}$ erg s^{-1}, well above the empirical threshold for generating a bright pulsar wind nebula ($\dot{E} \gtrsim 4 \times 10^{36}$ erg s^{-1}, Gotthelf 2004). Such young pulsars are often embedded in observable shell-type remnant which have yet to dissipate. However, like the Crab, G54.1+0.3 lacks evidence for a thermal remnant in any waveband (Lu et al. 2002). Most likely, the SN ejecta in these two remnants are still expanding into a very low density medium.

In this paper we present the first dedicated X-ray timing and spectral follow-up observations of PSR J1930+1852 since discovery. Previous X-ray results were based on archival data of limited quality. We use the new data to characterize the pulse shape and energy spectrum and provide a long term ephemeris. Throughout the paper, the uncertainties (statistical fluctuation only) are quoted at the 68% confidence level.

2. Observations and Data Analysis

The pulsar PSR J1930+1852 was observed twice with *RXTE* on 2002 September 12 – 14 and on 2002 December 23 – 25 using a combination of event and instrument modes. For consistency, we analyze the data taken with the proportional counter array (PCA) in the Good Xenon mode. PCA has a field of view of 1° (FWHM), total collecting area of about 6500 cm^2, time resolution of 1 μs, and spectral resolution of $\leq 18\%$ at 6 keV. The data are reduced and analyzed using the *ftools* software package version v5.2. We filter

the data using the standard $RXTE$ criteria, selecting time intervals for which parameters `Elevation_Angles` $< 10°$, `Time_Since_SAA` ≥ 30 min, `Pointing_Offsets` $< 0.02°$, and the background electron rate `Electron2` < 0.1. The effective exposure time after this filtering is 31.7 ks and 41.7 ks for the September and December observations. Since the background of $RXTE$ is high and the spectral resolution is relatively low, the $RXTE$ data is used herein exclusively for timing analysis, selecting photons detected from PCA PHA channels $0 - 35$ ($\sim 2 - 15$ keV). This results in a total of ~ 1 and ~ 1.6 million counts in the two observations for the subsequent analysis. The photon arrival times are corrected to the Solar system barycenter, based on the DE200 Solar ephemeris time system and the $Chandra$ J2000 coordinates of J193030.13+185214.1 (Lu et al. 2002).

SNR G54.1+0.3 was also observed with $Chandra$ on 2003 June 30 for a total of 58.4 ks. The pulsar was placed at the aim-point of the front-illuminated ACIS-I detector. The CCD chip I3 was operated in continuous-clocking mode (CC-mode), providing a time resolution of 2.85 ms and an one-dimensional imaging, in which the 2-D CCD image is integrated along the column direction in each CCD readout cycle. The photon arrival times are post-processed to account for the spacecraft dithering and SIM motion prior to the barycenter correction. The spectral data are corrected for the effects of CTI (Charge Transfer Inefficiency). However, the spectral gain is not well calibrated in the CC-mode, requiring adjustment in the fitting process (details are given in §3). Spectral response matrices are generated for the ACIS-I aimpoint, the location of the pulsar in this observation. After filtering the data using the standard criteria, the remaining effective exposure is 57.2 ks. Reduction and analysis of the $Chandra$ data are all based on the standard software package $CIAO$ (v3.2) and $CALDB$ (v3.0.0).

Figure 1 presents the geometry of the CC-mode observation overlaid on an archival $Chandra$ X-ray image of SNR G54.1+0.3. The CCD image is summed along the dimension perpendicular to the marked line which is orientated with a position angle $P.A. = 19°$ East of North. The count distribution along this dimension is shown in Figure 2. The central peak corresponds to the presence of the pulsar, which significantly contributes to the six adjacent pixels, as denoted by the upper horizontal bar. The neighboring four pixels (two on each side of the pulsar region), marked by the two lower horizontal bars, show the nearly same intensity level in the ACIS-I3 image-mode data with the pulsar excised. We therefore select counts falling in the inner six pixels for both our pulsar timing and spectral analysis of the pulsar, while those counts in the outer four pixels are used to estimate the background from the surrounding nebula.
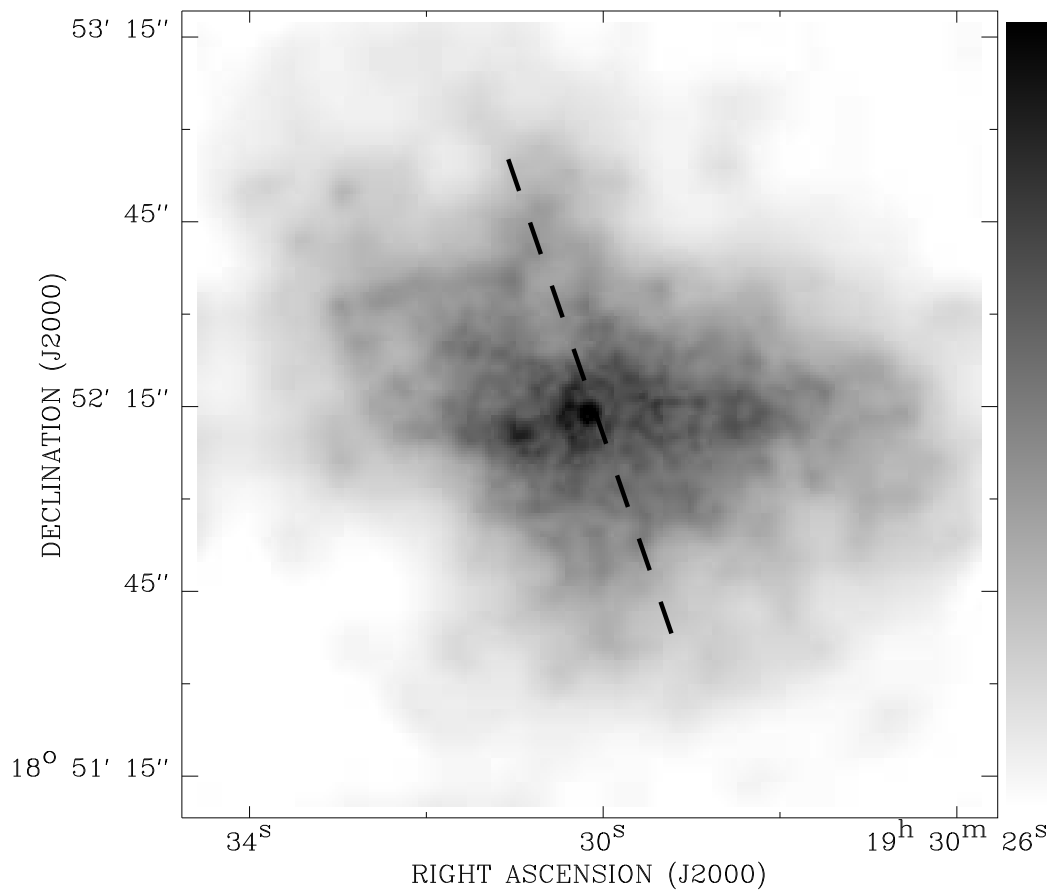
Fig. 1.— Geometry of the *Chandra* ACIS-I3 CCD continuous-clocking (CC-mode) observation of PSR J1930+1852 presented herein. The dashed line gives the orientation of the CC-mode observation shown overlaid on an archival *Chandra* broadband (0.3−10 keV) X-ray image of SNR G54.1+0.3.
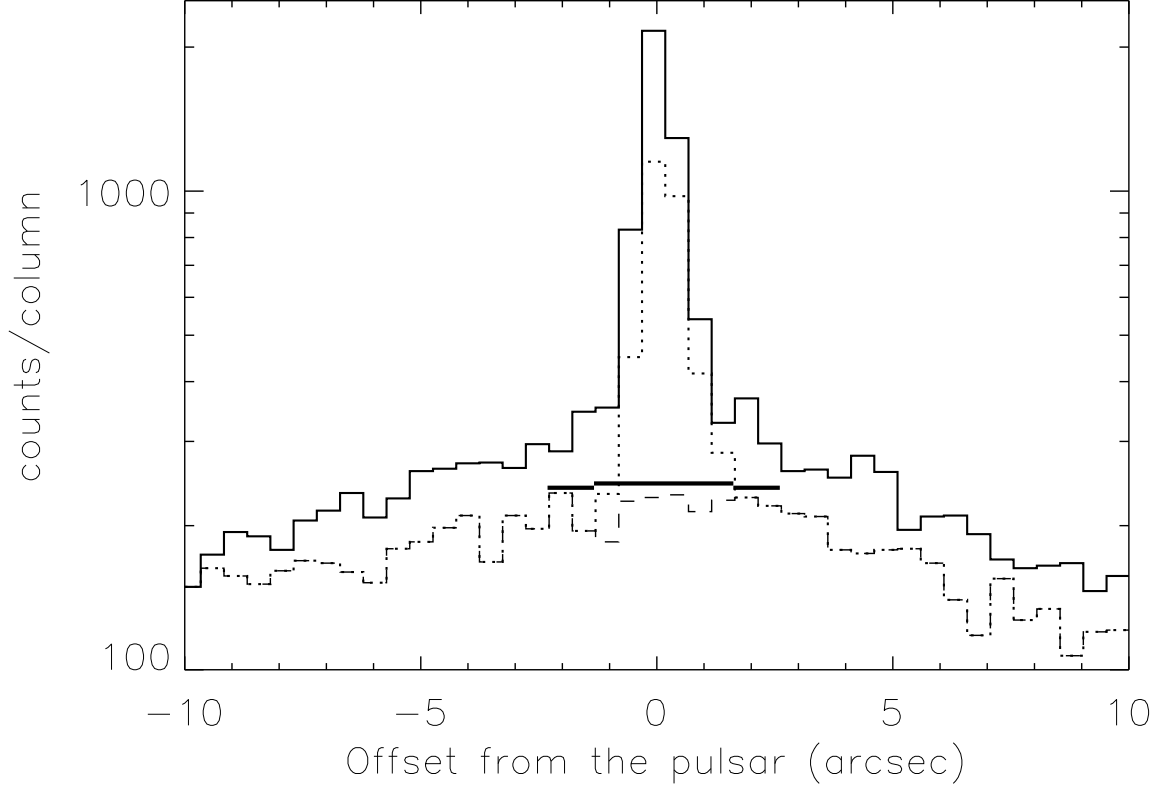
Fig. 2.— Source and background region determination for the *Chandra* CC-mode observation of PSR J1930+1852. The 1-D count distribution of SNR G54.1+0.3 as observed in CC-mode using ACIS-S3 (*solid line*), compared with the distributions constructed from the collapsed *Chandra* ACIS-I3 image-mode data, with (*dashed line*) and without (*dotted*) the pulsar excised. All data is restricted to the $0.3 - 10$ keV energy band. The on-pulsar (central) thick horizontal bar denotes the 6 pixels that contains significant pulsar emission, while the two adjacent off-pulsar (outer) thick horizontal bars mark the pixels that are used to estimate the local nebula background (see §2 for details).

3. Results

3.1. Pulsar Timing

For each observation, we search for the periodic signal of PSR J1930+1852 by folding events around the period extrapolated from the early radio ephemeris of Camilo et al (2002). For each period folding with a period P, a χ^2 is calculated from the fit to the pulse profile with a constant count rate. The null hypothesis of no periodic signal can be ruled out when a significant peak is seen in the resultant "periodogram" (χ^2 vs. P), which is the case for each of the X-ray observations at a high confidence ($\chi^2 > 300$ for 10 phase bins). We further fit the peak shape with a Gaussian profile to maximize the accuracy of our pulsar period determination (Figure 3). The centroid of this Gaussian is then taken as the best estimate of the pulsar period. The light curves derived of the *RXTE* and *Chandra* observations folded at the measured periods are shown in Figures. 4–5.

To estimate the uncertainties in the period measurements, we use the bootstrap technique of Diaconis & Efron (1983). This is done as the following: (1) constructing a new data set of the same total number of counts by re-sampling with replacement from the observed events; (2) determining the period with this re-sampled data set in the exactly same way as with the original data; (3) repeating the above two steps for 500 times to produce a period distribution; (4) Using the dispersion of this distribution as an estimate of the 1σ period uncertainty. The distributions produced for the three observations are shown in the right column of Figure 3, while the estimated uncertainties are included in Table 1.

To compute the pulsed fraction of the X-ray emission from PSR J1930+1852, we used the *Chandra* observation. We extracted a total of 5506 counts in the $0.3 - 10$ keV band from the on-pulsar pixels of the 1-D count distribution (the solid curve in Figure 2). After subtracting the local nebular contribution estimated from the neighboring off-pulsar pixels, the remaining 3560±92 counts are considered as the net total emission from the pulsar. This emission can be further divided into the pulsed and persistent components. To determine the persistent component, we construct a 1-D distribution of the persistent emission from the off-pulse counts, defined to be in the phase interval $0.1 - 0.3$ (Figure 5). The same on-pulsar pixels as shown in Figure 2 now contain a total of 598 counts, Corrected for the off-pulse phase fraction (1/5), the total number of persistent counts over the entire phase is then 598×5. Therefore, the net number of the pulsed counts is (5506-598×5)=2516±143. This results in a pulsed fraction of $f_p \equiv$ (pulsed/total counts) $= 71 \pm 5\%$.

3.2. Pulsed Emission Spectral Characteristics

To check for phase-dependent spectral variations across the pulse profile we compute the hardness ratio in each phase bin, defined as HR = N_h/N_s, where N_s and N_h are the counts selected from the $0.3 - 3$ keV and $3 - 10$ keV energy bands, respectively. The pulsar counts (pulsed and unpulsed) are extracted from the 6 pixel source region as discussed in §2 and the background from the neighboring 4 pixels. The calculated HR is shown in the lower panel of Figure 5. Fitting these HR data points assuming a constant HR value resulted in a χ^2 of 17.94 for 9 degrees of freedom, which means that the hardness ratio changes with phase at a confidence level of 96.4%. Further more, it appears that the HR values of the on pulse emission are higher than those of the off-pulse emission. In order to quantify this, we computed the mean HR for the off-pulse emission (bins 1, 2 3 and 10 in the panel) as HR = 0.77 ± 0.08 and the on-pulse bins (4 to 9) as HR = 0.95 ± 0.04. Therefore, the on-pulse emission is harder than the off-pulse emission at a confidence level of $\sim 2\sigma$, or 98%.

Next, we study the *Chandra* spectrum of PSR J1930+1852 using the same sources and background counts as extracted above. For the pulsed spectrum, the phase width corrected off-pulse counts are subtracted from the on-pulse counts in each spectral bin. Figure 6a presents the best fit absorbed power-law model using the standard response matrix. Although the overall χ^2 is acceptable (34.4 for 35 degree-of-freedom), the residuals to this fit display characteristic feature, indicating that the gain of the response function is not properly calibrated for the CC-mode. Following the method suggested by Kaaret et al. (2001) we calibrate the gain offset and scale in *XSPEC* by comparing the overall CC-mode spectra of PSR J1930+1852 to that determined by the ACIS-S3 imaging data. The latter is characterized by the same model with the absorption column density $N_H = 1.6 \times 10^{22}$ cm^{-2} and a photon index $\alpha = 1.35$ (Camilo et al. 2002). The resulting gain scale and offset are found to be 0.90 and -0.18, respectively. Fixing this gain correction and N_H to the above values, we re-fit the pulsed emission spectrum to obtain a photon index of 1.2 ± 0.2 (see Figure 6b). The new χ^2 value is 17.7 for 34 degree-of-freedom, significantly better than without the gain correction. The pulsed flux measured in the $2 - 10$ keV energy band is 1.2×10^{-12} ergs cm^{-2} s^{-1}. When compared to the overall $2 - 10$ keV flux of 1.7×10^{-12} ergs cm^{-2} s^{-1} (Camilo et al. 2002), this implies that $\sim 70\%$ of the total emission from the pulsar is pulsed, consistent with the estimate in Section 3.1.

4. Discussion

The properties of PSR J1930+1852 are most similar to those found for other examples of young, energetic pulsars. The power-law spectral index of the pulsar emission is consistent

with its spin-down energy according to the empirical law of Gotthelf (2003) for energetic rotation powered pulsars with $\dot{E} > 4 \times 10^{36}$ erg s^{-1}. The power law index is also consistent with that of the pulsed emission, as found for other high $\dot{E}$, Crab-like pulsars (Gotthelf 2003). As with most X-ray detected radio pulsars, the X-ray pulse morphology differs from that of the radio pulse. The full width at half maximum (FWHM) of the X-ray pulse is 0.4 phase compared to 0.15 phase in radio. Notably, the X-ray pulse has a steep rise and slow decline, whereas the radio pulse is inverted, with a slow rise and steep decay instead.

The unpulsed component of PSR J1930+1852 is most likely nonthermal in nature as the thermal emission from the cooling surface of the neutron star should be negligible. According to the standard theoretical cooling curves, the surface temperature of a 1.4 M$\odot$ neutron star is about 0.13 keV at the age of PSR J1930+1852 (about 3,000 years; Page 1998). Assuming a radius of 12 km the neutron star should have an absorbed $0.2 - 10$ keV flux of $\sim 8 \times 10^{-15}$ erg cm^{-2} s^{-1}, which accounts for $\sim 0.4\%$ of our detected total $0.2 - 10$ keV X-ray flux or 1.4% of the unpulsed flux. Tennant et al. (2001) detected the X-ray emission of the Crab pulsar at its pulse minimum, though accounting for only a tiny fraction of the total or unpulsed flux. Tennant et al. (2001) further suggested that this component is nonthermal. The unpulsed X-ray emission from PSR J1930+1852 may be of the same nature as that of the Crab pulsar.

Together with the previous X-ray and radio periods, the three timing measurements obtained herein provide an opportunity to study the pulsar period evolution. A linear fit to these periods yields a $\dot{P}$ of 7.5116(6)$\times 10^{-13}$ s s^{-1} with a reduced χ_ν^2 of 3.6 (see Figure 7). The large χ_ν^2 value and the scattered residuals show that the period of PSR J1930+1852 evolves in a more complicated than a simply constant spin down. The period derivative obtained here is also significantly (9σ) different from that obtained by Camilo et al. (2002). This suggests that PSR J1930+1852 has experienced periods of timing noise and/or glitches - not unepxected for a young pulsar (e.g., Zhang et al. 2001; Wang, et al. 2001; Crawford & Demiańsky 2003). Arzoumanian et al. (1994) defined a quantity Δ_8 to represent the stability of a pulsar. They found an empirical relation between Δ_8 and $\dot{P}$, which predicts a high Δ_8 of -0.67 for PSR J1930+1852. This value is higher than those measured for most ordinary pulsars and is consistent with the variability in spin-down rate observed for this pulsar.

Indeed, PSR J1930+1852 shares other interesting properties with PSR B0540-69. For example, the pulsed X-ray emission of PSR B0540-69 has probably a harder spectrum, with a photon index of 1.83$\pm$0.13, than the steady component whose photon index is (2.09$\pm$0.14; Kaaret et al. 2001), whereas PSR J1930+1852 also has a harder pulsed emission than the steady emission. Furthermore, the pulse width of PSR B0540-69 is about 0.4 and its pulsed

fraction $f_p = 71.0 \pm 5\%$, both nearly identical to the respective values measured herein for PSR J1930+1852. Based on these X-ray emission similarities, the X-ray emission regions of the two pulsars may have the similar overall structures and viewing geometries.

REFERENCES

Arzoumanian, Z., Nice, D.J., Taylor, J.H., & Thorestt, S.E. 1994, ApJ, 422, 671

Camilo, F., Lorimer, D.R., Bhat, N.D.R., Gotthelf, E.V., Halpern, J.P., Wang, Q.D., Lu, F.J., & Mirabal, N. 2002, ApJ, 574, L71

Crawford, F., & Demiański, M. 2003, ApJ, 595, 1052

Diaconis, P., & Efron, B. 1983, Scientific American, May P96

Gotthelf, E. V. 2003, ApJ, 591, 361

Gotthelf, E. V. 2004, in "Young Neutron Stars and Their Environments", IAU Symp. 218. Ed. F. Camilo & B. M. Gaensler (S.F. CA.: ASP) 2004, 218, 225

Kaaret, P., et al. 2001, ApJ, 546, 1159

Lu, F.J., Wang, Q.D., Aschenbach, B., Durouchoux, P., & Song, L.M. 2002, ApJ, 568, L49

Middleditch, J., et al. 2006, ApJ, 652, 1531

Page, D. 1998, in The Many Faces of Neutron Stars ed. R. Buccheri, J. van Paradijs, & M.A. Alpar (Dordrecht: Kluwer), 539

Tennant, A.F., et al. 2001, ApJ, 554, L173

Wang, N., Wu, X.J., Manchester, R.N., et al. 2001, Chin. J. Astron. Astrophys., 1, 195

Zhang, W., Marshall, F.E., Gotthelf, E.V., Middleditch, J., & Wang, Q.D. 2001, ApJ, 554, L177
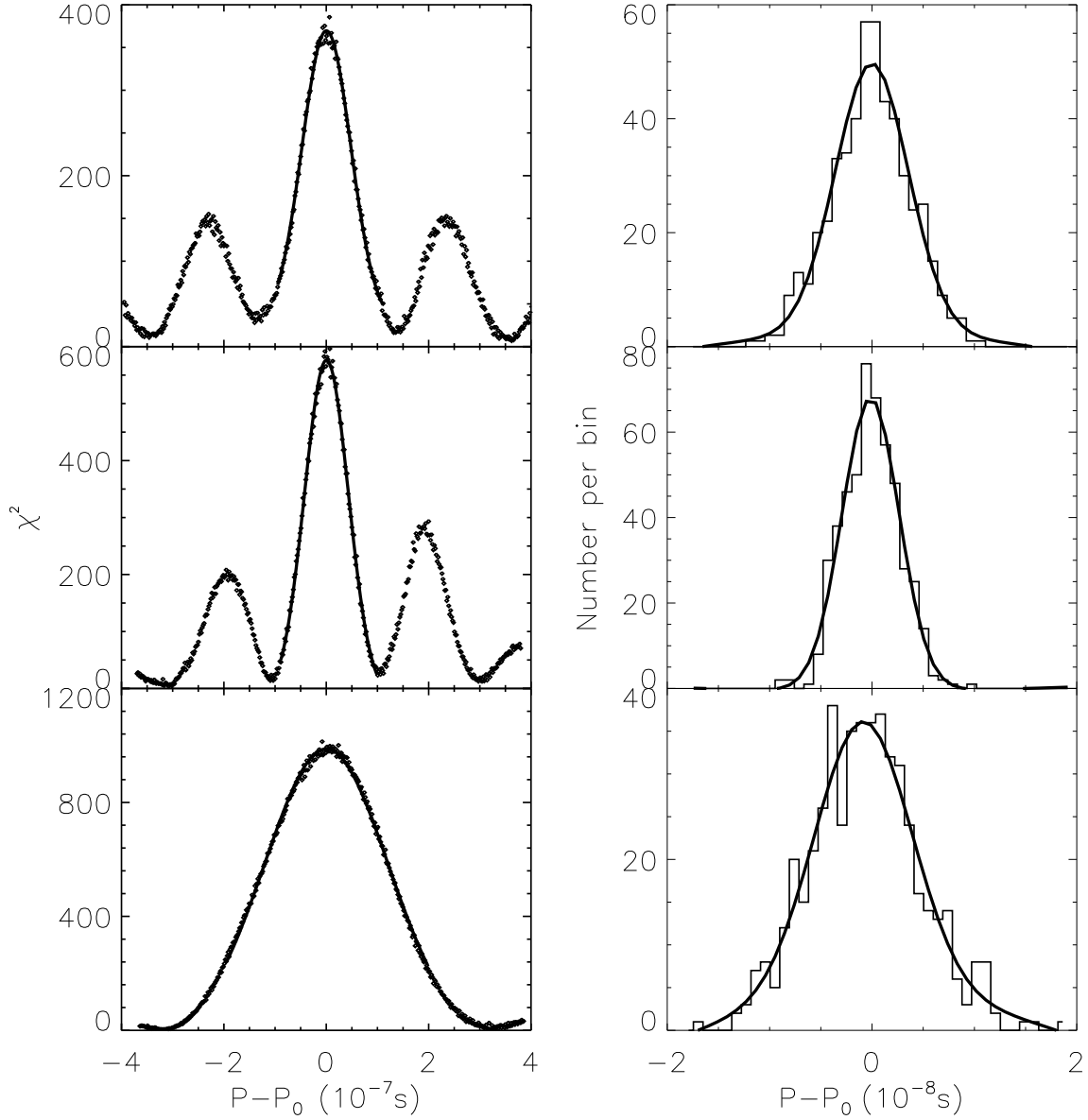

Fig. 3.— Period and period uncertainty of PSR J1930+1852 at three epochs. *Left* – The periodograms of PSR J1930+1852 constructed from the September 2002, December 2002, and June 2003 observations and together with the respective best-fit Gaussian profiles for the central peaks. *Right* – The distribution of the 500 periods from the bootstrapped data for each observations. The Gaussian 1σ width gives an estimate of the period uncertainty. The P_0 values are given in Table 1.
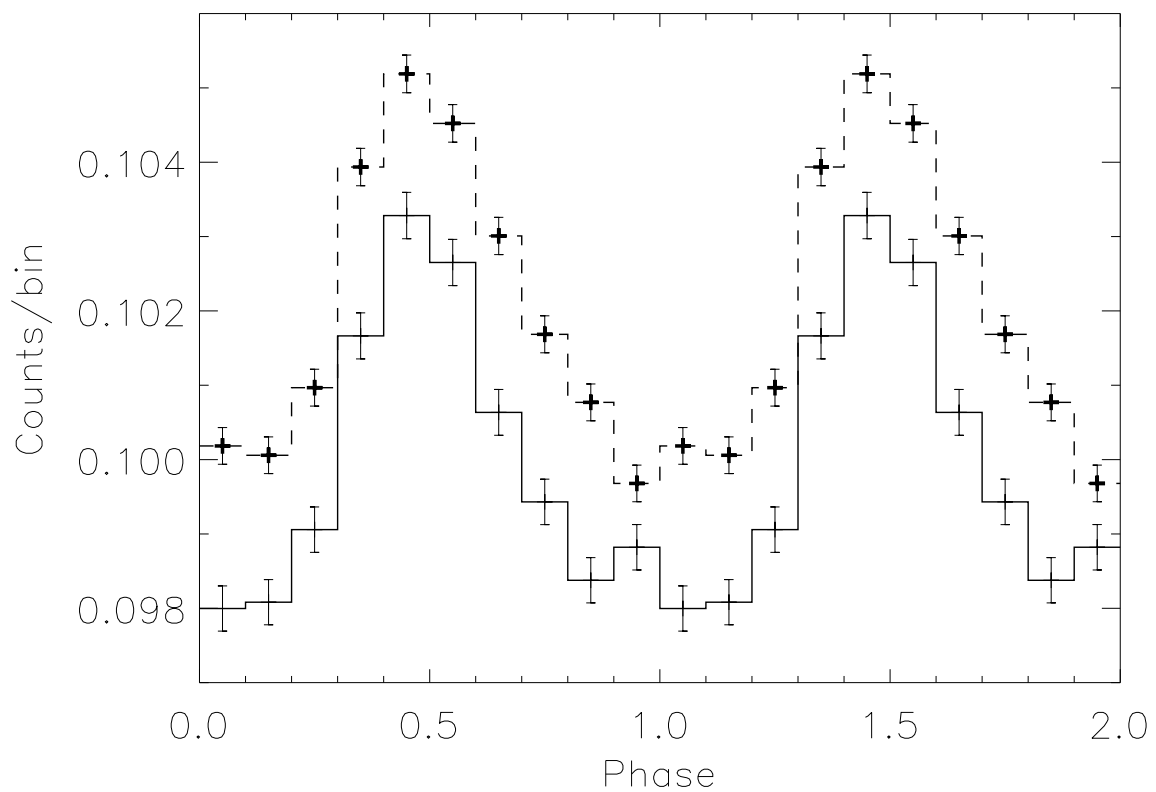
Fig. 4.— The pulse shape of PSR J1930+1852 in the $2 - 15$ keV band as obtained with *RXTE* on 2002 September 12 (solid) and December 23 (dashed). Phase zero is arbitrary; two cycles are shown for clarity. The December light curve is shifted upward by 0.002.
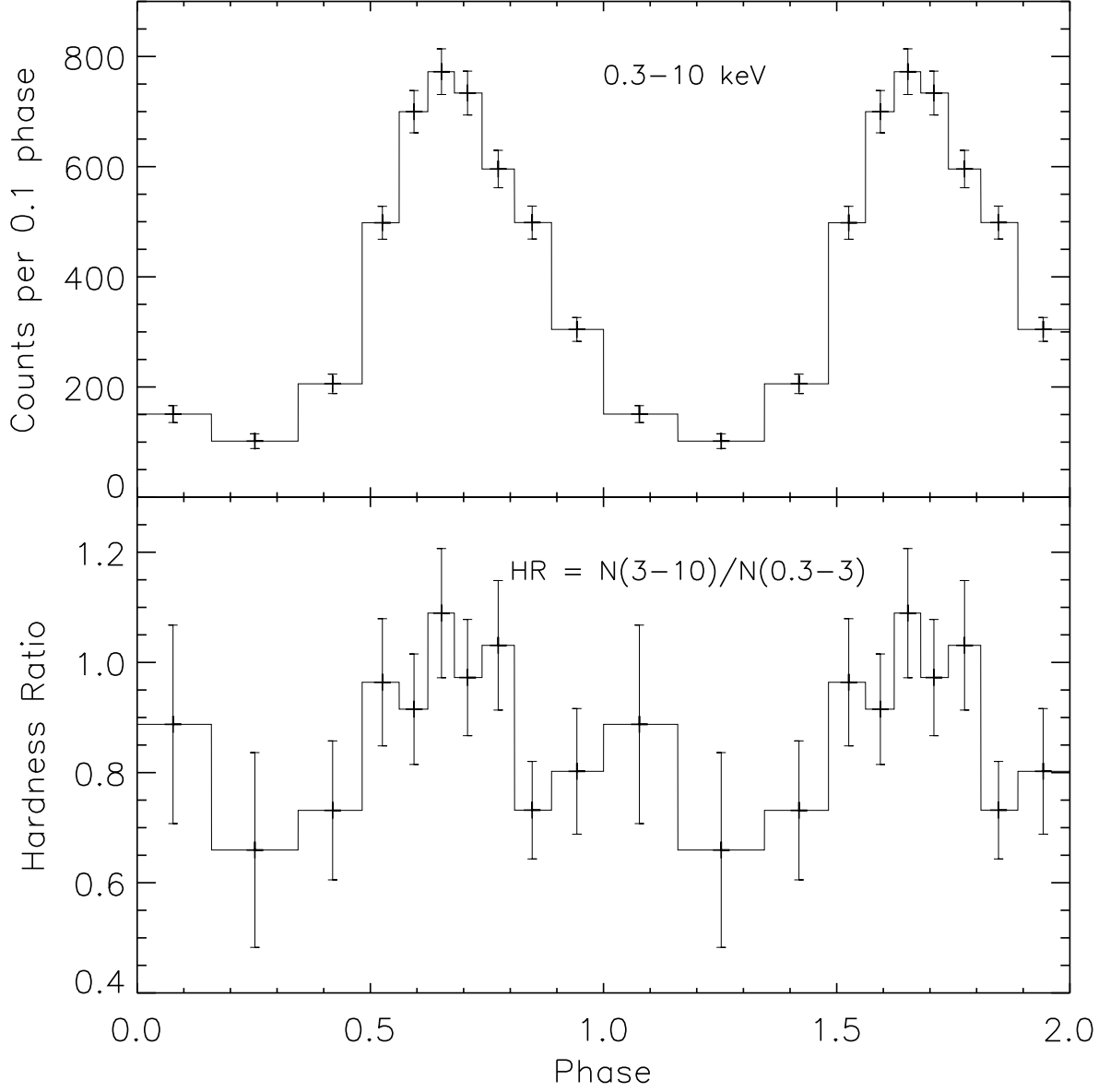
Fig. 5.— The pulse shape and its hardness ratio of PSR J1930+1852 in the $0.3 - 10$ keV band as measured with *Chandra* on 2002 June 30. The pulse shape (*Top Panel*) is folded at the period given in Table 1 and the phase bin size is chosen so that each bin contains almost the same counts. The hardness ratio (*Bottom Panel)* is as defined in the text (§3.2); the background, as defined in §2, has been subtracted.

Table 1.   Timing Results for PSR J1930+1852

Date (UT)	Obs. Type	Epoch (MJD[TDB])	Period (s)
1997 Apr 27	ASCA	50566	0.13674374(5)[a]
2002 Jan 17	Radio	52280	0.136855046957(9)[a]
2002 Sep 12	RXTE	52530	0.136871312(4)
2002 Dec 23	RXTE	52632	0.136877919(3)
2003 Jun 30	Chandra	52820	0.136890130(5)

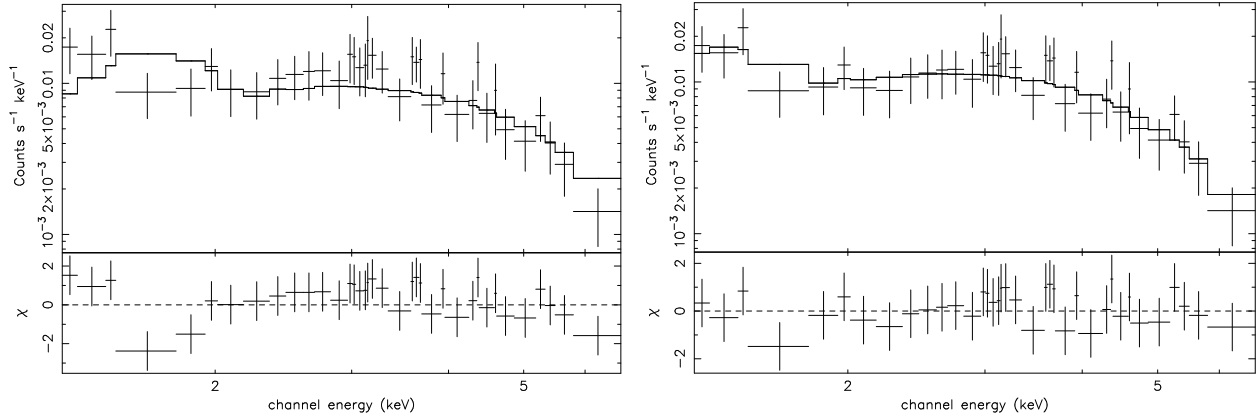[a]Taken from Camilo et al. (2002)

Fig. 6.— The pulsed X-ray spectrum of PSR J1930+1852 obtained with *Chandra* ACIS-I3 in continuous-clocking mode: *Left Panel:* fitting with an absorbed power-law model with the gain scale and offset fixed as 1 and 0; *Right Panel:* fitting with the same model but with the gain scale and offset of 0.90 and -0.18.
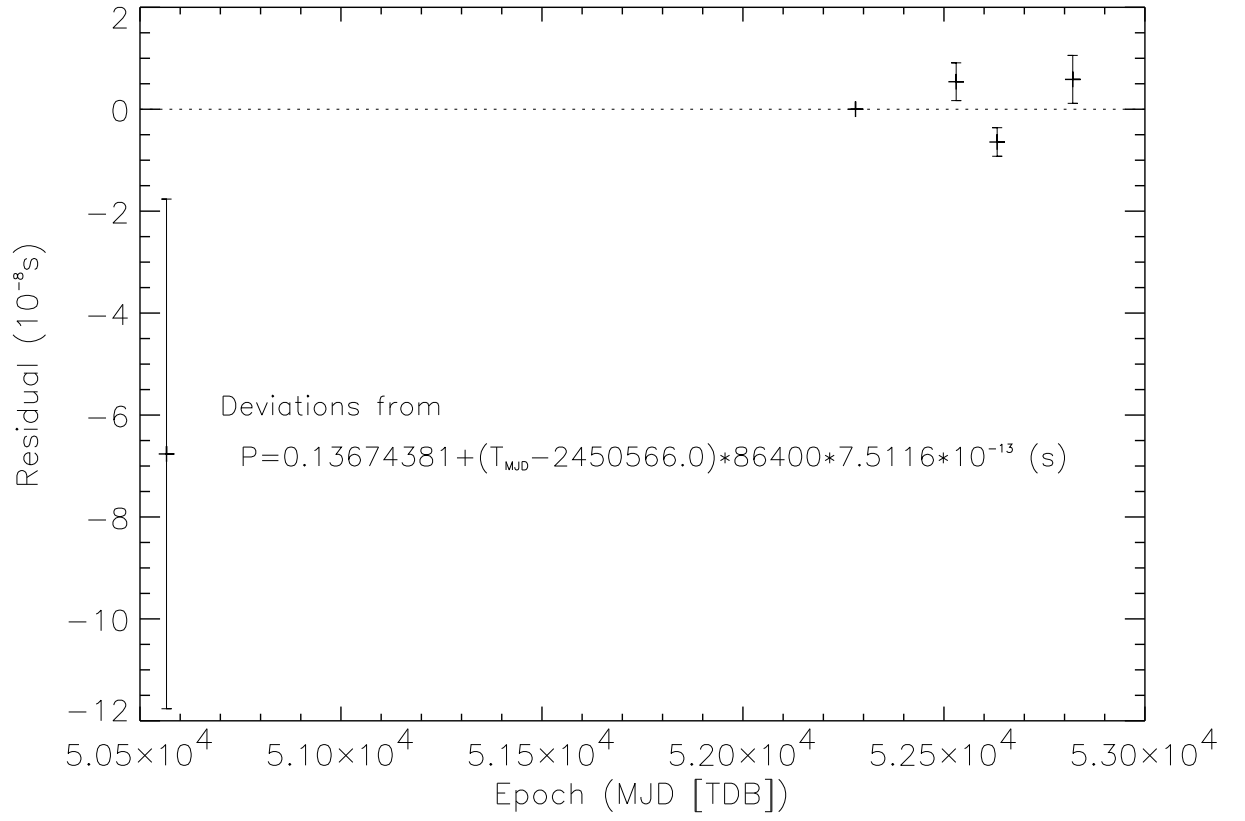
Fig. 7.— The period residuals of PSR J1930+1852 in different epochs.